International Journal of Computational Methods
(2025) 2441007 (16 pages)

DOI: 10.1142/S021987622441007X

Numerical Study of Hydrodynamic and Thermal Wake Flows around an Underwater Vehicle

Gang Gao [*], Yangjun Wang [†], Liushuai Cao [*] and Decheng Wan [*,‡]

[*] *Computational Marine Hydrodynamic Lab (CMHL)*
School of Naval Architecture, Ocean and Civil Engineering
Shanghai Jiao Tong University, Shanghai, P. R. China

[†] *College of Advanced Interdisciplinary Studies*
National University of Defense Technology
Nanjing, P. R. China
[‡] *dcwan@sjtu.edu.cn*

Received 31 October 2024
Accepted 27 March 2025
Published 6 May 2025

During the movement of underwater vehicles, hydrodynamic wakes are formed along with long-distance thermal wakes caused by the release of thermal wastewater. By capturing and imaging the thermal wake generated behind the underwater vehicle in real time, it is possible to determine the size, speed, and location of the vehicle. Investigating the hydrodynamic wake and thermal wake of underwater vehicle requires the integration of various physical fields, including fluid mechanics and temperature. Current research is centered on analyzing the impact of factors like the underwater vehicle's speed, temperature and flow rate of thermal wastewater on the wake. However, there is a lack of comprehensive studies in this area, as well as limited attention given to the effects of attachments and propellers on thermal wake. This study conducted numerical simulations using the RANS method to analyze the hydrodynamic and thermal wake of an underwater vehicle with a fully attached body. The research considered various speeds, propeller speeds, temperatures and flow rates of thermal wastewater. The results revealed that the propeller significantly influences the core region of the thermal wake. The temperature decays rapidly when closer to the vehicle and slower at greater distances. Moreover, higher speeds and propeller rotation speeds lead to a larger affected area by temperature. Additionally, increasing the temperature and flow rate of thermal wastewater strengthens the thermodynamic signal in the wake behind the underwater vehicle.

Keywords: Hydrodynamic wake; thermal wake; numerical simulation; underwater vehicle; thermal wastewater.

1. Introduction

The continuous operation of the engine is used to propel underwater vehicles, while cooler water within the vehicle is employed to cool the heating engine. This water,

---

[‡] Corresponding author.

after absorbing heat from the engine, experiences a temperature increase. The underwater vehicle then discharges this heated wastewater into the surrounding environment. The thermal waste water exchanges heat with the ambient water, creating a thermal signal behind the underwater vehicle and at the free surface. Cao *et al.* [2023, 2024] pointed out that this thermal signal can be detected by infrared equipment, which allows for the estimation of the underwater vehicle's size, position, and speed. Utilizing thermal signals for such detection has become a crucial method for identifying and tracking underwater vehicles.

There has been significant research on the hydrodynamic and thermal wakes generated by underwater vehicles. In an experimental study, Luo *et al.* [2024] established a testing platform in an outdoor pool to investigate the thermal wake of underwater vehicles. Using infrared imaging, obtained parameters and images of the thermal wake at the water surface. Results revealed that vortices of different scales within the wake interact with the water surface's thermal boundary layer, leading to modulation, amplification, and dispersion effects that result in variations in temperature characteristics. Similarly, Wang *et al.* [2023] conducted experiments to analyze the effects of parameters such as Reynolds number, submersion depth, propeller speed, thermal jet, and temperature difference on the temperature distribution at the free surface. Findings indicated that the infrared signals on the water surface are not direct thermal signals generated by the buoyancy of the thermal wake. Also, observed that the area of temperature signal on the water surface increases with greater submersion depth. Li *et al.* [2023] developed an experimental platform for investigating thermal wakes using a scaled-down Suboff model. Through tests of straight-line motion and thermal discharge, characterized the temperature distribution at the free surface.

Experimental studies on underwater vehicles predominantly use scaled models, as conducting full-scale experiments under laboratory conditions poses significant challenges. In terms of numerical simulations, Luo *et al.* [2023] developed a thermal wake computation model based on the Detached Eddy Simulation (DES) method. And investigated the interaction between the hydrodynamic wake and the temperature boundary layer, focusing on thermal diffusion and heat transfer at the interface. Findings indicated that the thermal wake on the free surface exhibits a distinct elongated vortex structure. Gu *et al.* [2018] utilizing the Volume of Fluid (VOF) method and overset grid technique, simulated the thermal wake of an underwater vehicle under conditions of density and temperature stratification. And discovered that both thermal and hydrodynamic wakes could manifest on the free surface. In deeper regions, colder water was observed to ascend to the surface due to the disturbance caused by the underwater vehicle, forming a cold wake.

Zhang *et al.* [2019] employed the finite volume method to analyze the impact of submersion depth, speed, and propeller rotation on the thermal wake using the LSII submarine model. Results demonstrated that disturbances in cold seawater at greater depths lead to the formation of a cold wake. The interaction of cold and thermal wakes creates a unique downstream surface pattern characterized by alternating cold and warm wakes. Huang *et al.* [2024] established a coupled model of flow and electromagnetic fields to study the evolution of the far-field wake magnetic field of a full-scale submarine. Chen *et al.* [2023] developed an interdisciplinary model incorporating continuity, momentum, heat, mass, and Maxwell's equations to conduct numerical simulations of the velocity, vorticity, and electromagnetic field distribution in the far field of a full-scale submarine. Luo *et al.* [2022] further investigated the effects of thermal jets on the water body, discovering that thermal conduction, convection, and entrainment contribute to the presence of thermal signals, cold-thermal signals, and cold signals across different water layers. The boundaries and distribution range of these signals in various layers are determined by the parameters of the thermal jet and the submersion depth.

It is evident that both experimental and numerical simulation studies have predominantly focused on observing thermal signals near the free surface. There is relatively less attention given to the thermal signals behind underwater vehicles at greater depths. Furthermore, most research has been conducted using scaled models rather than full-scale underwater vehicles. This study addresses the thermal wake of a full-scale underwater vehicle with complete appendages. Based on the Reynolds-Averaged Navier–Stokes (RANS) method, conducted numerical simulations under various conditions, including different vehicle speeds, propeller rotations, and thermal wastewater temperatures and flow rates. The structure of this paper is as follows: begin with an introduction to the numerical simulation methods employed in this study. And then present the computational results for typical scenarios, followed by a discussion of the corresponding conclusions.

2. Numerical Method

2.1. *Governing equations*

In the solution process of this paper, the fluid motion satisfies the mass conservation and momentum conservation equations.

$$\nabla \cdot \mathbf{U} = 0, \tag{1}$$

$$\frac{\partial \rho \mathbf{U}}{\partial t} + \nabla \cdot (\rho \mathbf{U}\mathbf{U}) = -\nabla p + \rho g + \nabla \cdot (\mu \nabla \mathbf{U}), \tag{2}$$

where $\mathbf{U}$ is the velocity field, ρ is the density of fluid, p is the pressure field, g is the gravity acceleration, and μ is the dynamic viscosity coefficient. The turbulence model used $SST\ k - \omega$ model.

2.2. *Geometric model*

The SUBOFF (Submarine Fully Appended) model used in this study is a standardized submarine model developed by the U.S. Defense Advanced Research Projects Agency (DARPA), providing reliable comparative data for numerical simulations. The model consists of a streamlined hull, an outer shell, and four symmetrical tail

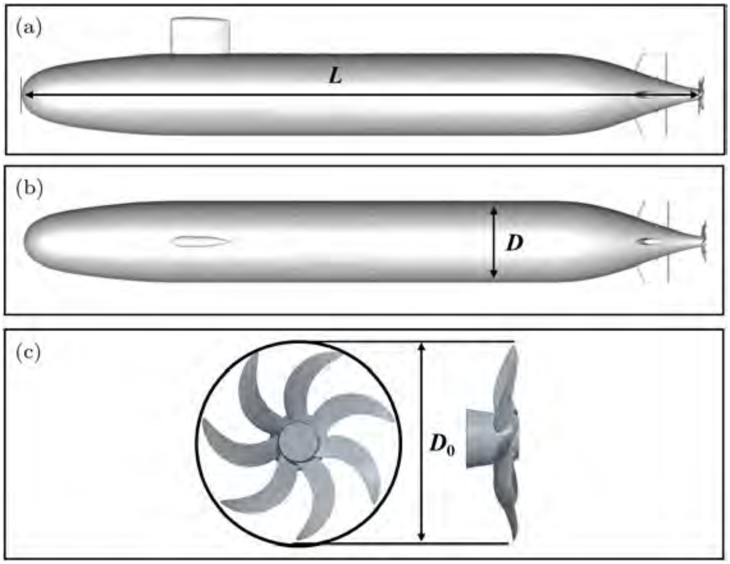

Fig. 1. The SUBOFF fully appended submarine model.

Table 1. Main parameters of the submarine-propeller system at full scale.

Parameter	Symbol	Unit	Value
Hull length	L	m	100.188
Hull diameter	D	m	11.684
Propeller diameter	D_0	m	9.564
Number of blades	N	—	7

fins. It has a length of 4.356 m and a diameter of 0.508 m. For this study, the model is scaled up by a factor of 23, and the propeller is modeled using the E1619 propeller model. The geometric representation of the model is shown in Fig. 1, and Table 1 lists the key parameters of the SUBOFF submarine and the propeller.

2.3. *Computational domain setup*

The computational domain setup is illustrated in Fig. 2. The inlet of the computational domain is positioned $1L$ upstream from the nose of the underwater vehicle. The lateral boundaries are set $1.5L$ from the sides of the vehicle. The outlet is placed $11L$ downstream from the stern of the vehicle. The top boundary is located $1L$ above the vehicle, while the bottom boundary is $0.5L$ below the vehicle.

2.4. *Mesh generation*

As shown in Fig. 3, local grid refinement is applied in regions with high surface curvature on the underwater vehicle and near the thermal discharge port. Additionally,

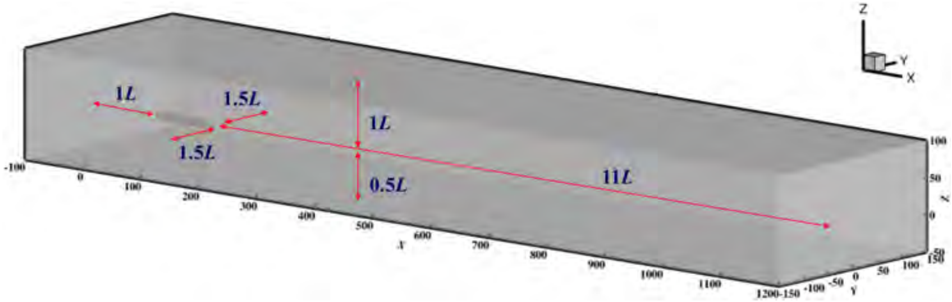

Fig. 2. Computational domain setup.

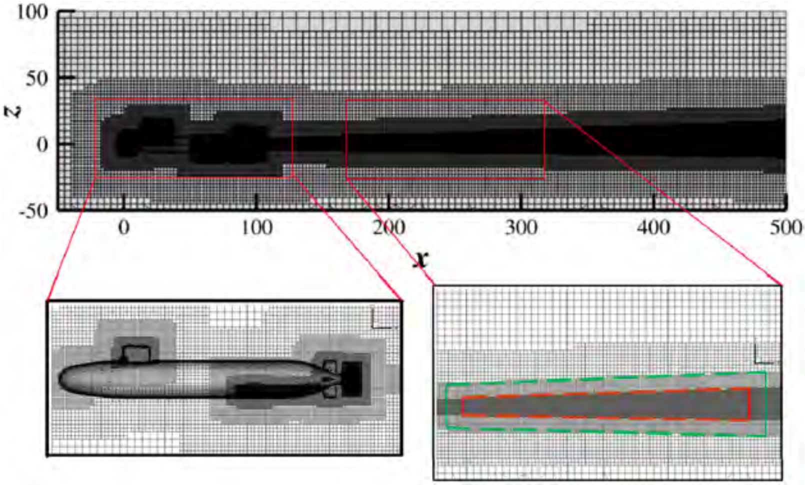

Fig. 3. Computational mesh.

a conical refinement is implemented in the wake region to account for the upward movement of the wake during its development.

2.5. *Boundary condition*

In terms of boundary condition settings, the inlet of the computational domain is defined as a velocity inlet boundary, and the outlet is set as a pressure outlet boundary. The lateral and vertical boundaries of the computational domain are all specified as velocity inlet boundaries.

2.6. *Computational conditions setup*

As shown in Table 2, the operating conditions for the calculations in this study are presented, including the velocity of the underwater vehicle, the rotational speed of

Table 2. Computational conditions.

Case	The speed of underwater vehicles (kn)	The speed of the propeller (rpm)	Temperature difference (K)	Flow rate (t/h)	The temperature of the background (K)
1	6	42	14	450	277.51
2	12	84	17	900	277.51
3	18	126	20	1350	277.51
4	30	210	23	2250	277.51

the propeller, the temperature and flow rate of the thermal discharge water, and the temperature of the ambient seawater.

3. Results and Discussions

3.1. *The temperature distribution in the wake*

First, the changes in temperature distribution in the wake at different cruising speeds were compared, as illustrated in Fig. 4. The figure presents the variation curves of the maximum temperature at various positions behind the underwater vehicle under different cruising speeds. Due to the initial condition settings, it can be observed that as the cruising speed increases, the maximum temperature also rises. Additionally, as the distance from the vehicle increases, the maximum temperature decreases for all cruising speeds. The rate of temperature decay becomes more pronounced with higher cruising speeds at larger distances.

Figures 5 and 6, respectively, show the temperature distribution on the $z = 0$ and $y = 0$ planes. It is evident that the temperature decreases as the distance from the underwater vehicle increases. In terms of the distribution range, the vertical temperature distribution spans a greater extent compared to the lateral distribution.

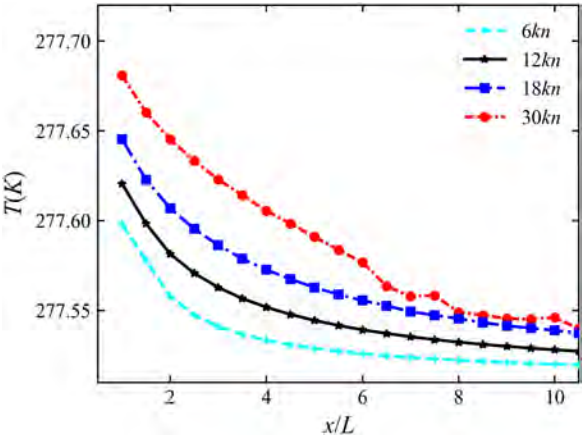

Fig. 4. Temperature maximum value variation curve of the wake.

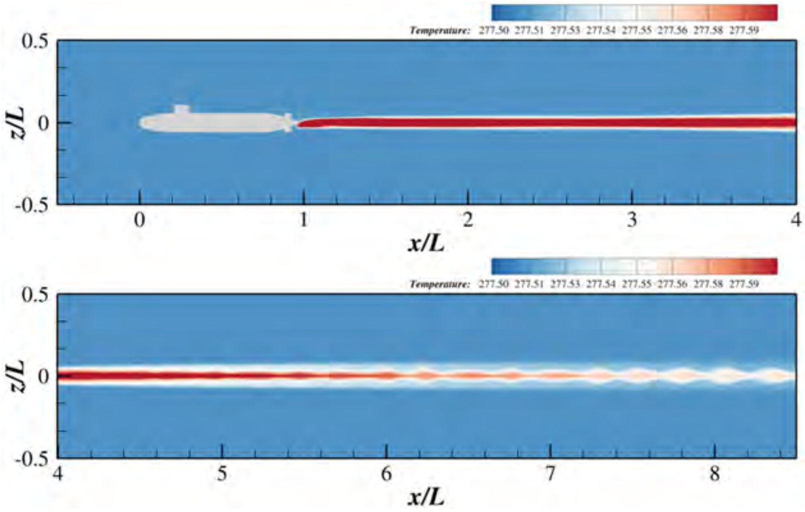

Fig. 5. Temperature distribution of the wake ($z = 0, 30\,\mathrm{kn}$).

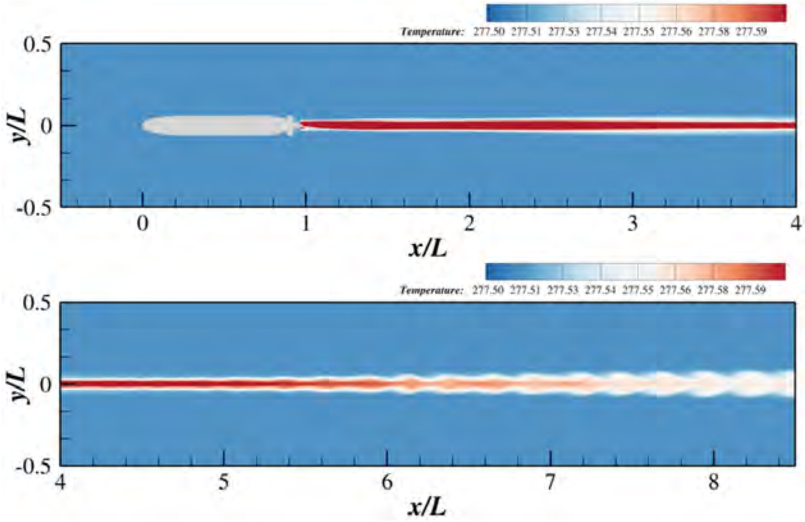

Fig. 6. Temperature distribution of the wake ($y = 0, 30\,\mathrm{kn}$).

Moreover, as the distance from the underwater vehicle increases, the temperature distribution in the wake begins to exhibit oscillations. For example, within the range of $(x/L > 6)$, a spindle-shaped distribution pattern starts to emerge.

Figure 7 presents the three-dimensional structure of the temperature iso-surface, specifically set at $277.55\,\mathrm{K}$. Upon closer examination of the enlarged local view, it

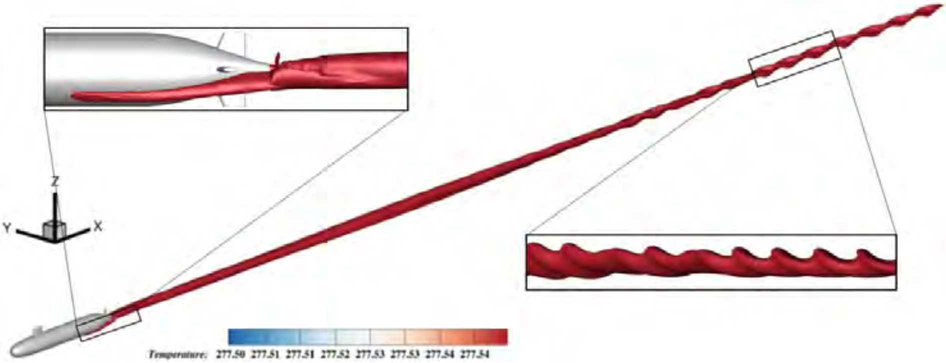

Fig. 7. Temperature iso-surface of the wake ($T = 277.55\,\mathrm{K}$, 30 kn).

becomes evident that these iso-surface primarily depict the thermal wake generated by the thermal discharge from the underwater vehicle's outlet. As the distance from the underwater vehicle increases, the overall shape of the iso-surface exhibits a spiraling pattern. Observing the temperature distribution plots of different sections behind the underwater vehicle in Fig. 8, it is noticeable that as the distance increases, the temperature values in the wake gradually decrease. Simultaneously, the area affected by the temperature of the wake expands. Between $x/L = 3$ and $x/L = 7$, the temperature distribution in the wake forms two trailing vortex tips, closely resembling the topology of the propeller. This indicates the significant influence of the propeller on the temperature distribution of the wake. However, from $x/L = 8$ to $x/L = 9$, the variation in the temperature distribution of the wake becomes minimal, suggesting a reduced disturbance effect of the propeller in this range.

3.2. *The velocity distribution in the wake*

Subsequently, the variations in velocity distribution in the wake at different cruising speeds were compared. Figure 9(a) presents the curves depicting the changes in maximum velocity at various positions behind the underwater vehicle under different cruising speeds. It is evident that as the cruising speed increases, the maximum velocity also increases. Additionally, as the distance increases, the maximum velocity decreases gradually for all cruising speeds. Figure 9(b) illustrates the normalized velocity variation curves, showing that with increasing cruising speed, the decay rate of maximum velocity becomes more pronounced at larger distances.

Figures 10 and 11, respectively, illustrate the velocity distributions on the $z = 0$ and $y = 0$ planes. It can be observed that the velocity values decrease as the distance from the underwater vehicle increases. Similarly, in terms of distribution range, the vertical distribution of velocity spans a significantly larger extent compared to the lateral distribution. Furthermore, as the distance from the underwater vehicle increases, the velocity distribution in the wake begins to exhibit oscillations. For

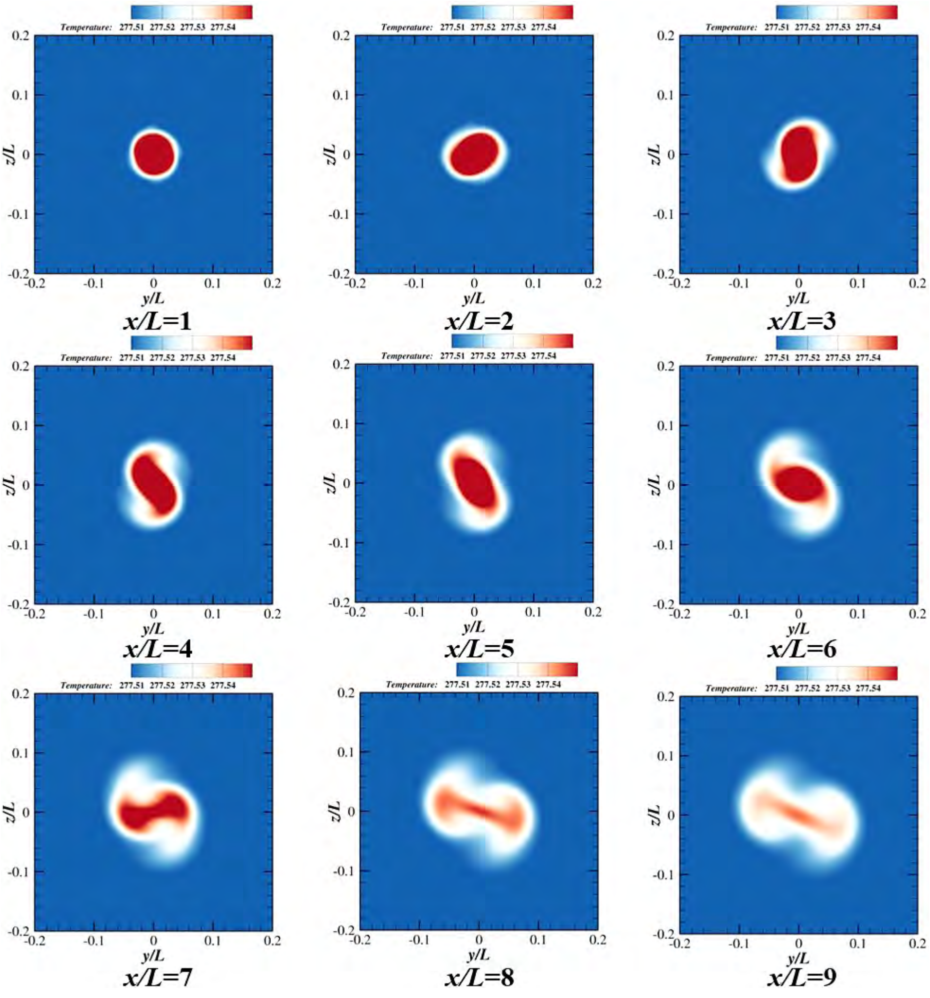

Fig. 8. Distribution of temperature (30 kn).

instance, within the range of $x/L > 6$, a spindle-shaped distribution pattern also emerges.

Figure 12 depicts the three-dimensional structure of velocity iso-surface, set at a value of 18 m/s. Upon closer examination of the enlarged local view, it becomes evident that the iso-surface expands gradually when closer to the underwater vehicle, while assuming a spiraling pattern as the distance from the underwater vehicle increases. Figure 13 illustrates the velocity distribution plots of different sections behind the underwater vehicle. It can be observed that as the distance increases, the velocity values in the wake gradually decrease. Simultaneously, the area affected by the wake's velocity expands. Between $x/L = 3$ and $x/L = 7$, the velocity distribution in the wake exhibits two trailing vortex tips, resembling the topology of

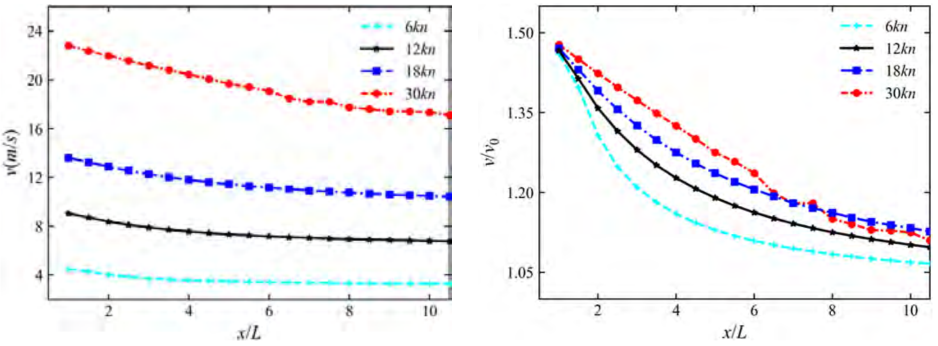

(a) (b)

Fig. 9. Velocity maximum value variation curve of the wake.

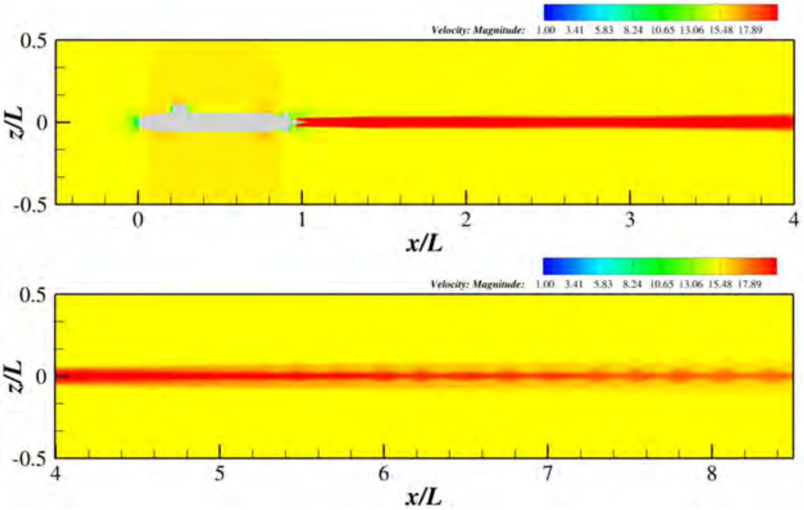

Fig. 10. Velocity distribution of the wake ($z = 0, 30\,\text{kn}$).

the propeller. This indicates a significant influence of the propeller on the velocity distribution of the wake. However, from $x/L = 8$ to $x/L = 9$, the variation in the velocity distribution of the wake becomes minimal, suggesting a reduced disturbance effect of the propeller in this range.

3.3. *The vorticity distribution in the wake*

Subsequently, the variations in vorticity distribution in the wake at different cruising speeds were compared. Figure 14(a) presents the curves depicting the changes in maximum vorticity at various positions behind the underwater vehicle under different cruising speeds and propeller rotational speeds. It can be observed that as the

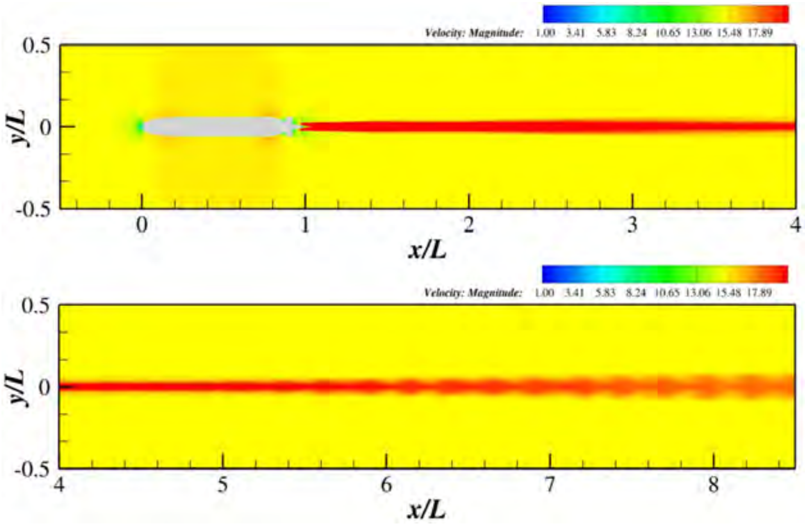

Fig. 11. Velocity distribution of the wake ($y = 0, 30\,\text{kn}$).

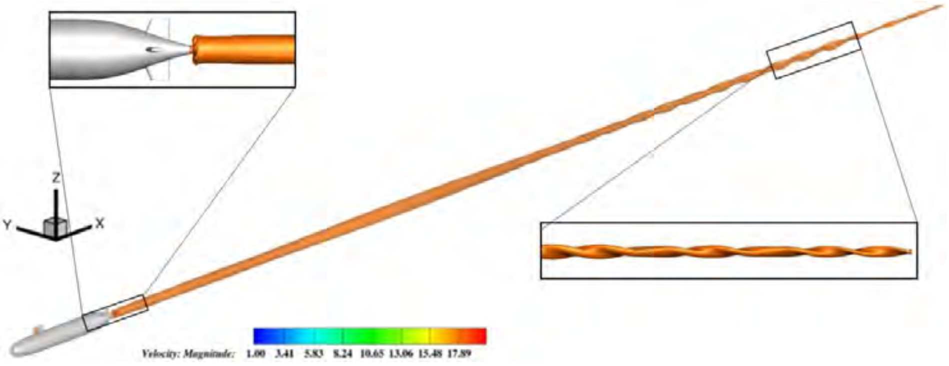

Fig. 12. Velocity iso-surface of the wake ($v = 18\,\text{m/s}$, $30\,\text{kn}$).

cruising speed and propeller rotational speed increase, the maximum vorticity also increases. Additionally, as the distance increases, the maximum vorticity decreases gradually for all cruising speeds. Figure 14(b) illustrates the normalized vorticity variation curves, showing that with decreasing cruising speed, the decay rate of maximum vorticity becomes more pronounced at larger distances.

Figures 15 and 16, respectively, illustrate the velocity distributions on the $z = 0$ and $y = 0$ planes. It can be observed that the velocity values decrease as the distance from the underwater vehicle increases. For instance, within the range $x/L > 4$, the maximum vorticity in the wake predominantly surrounds the underwater vehicle rather than being concentrated along its axis.

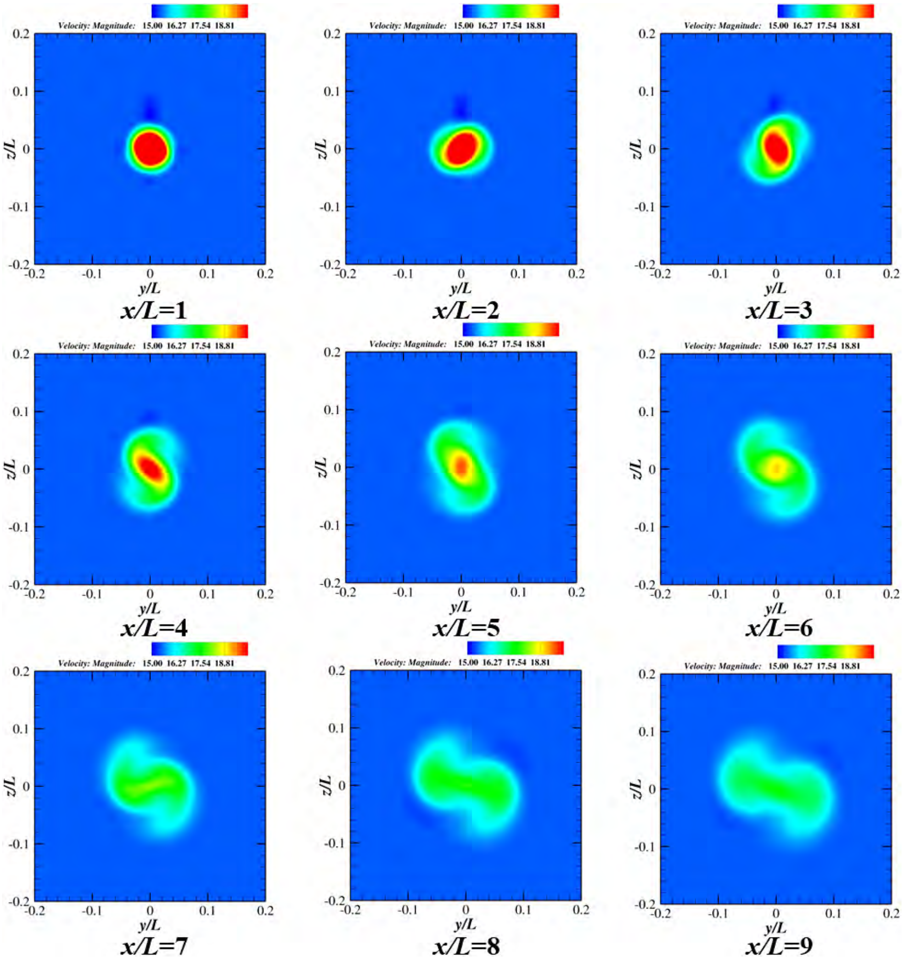

Fig. 13. Distribution of velocity (30 kn).

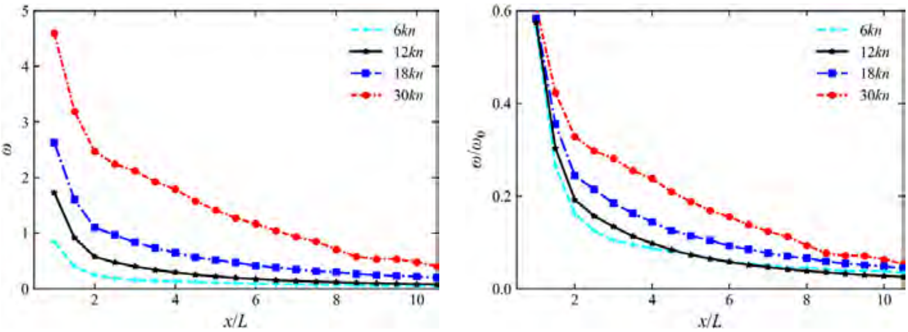

(a)

(b)

Fig. 14. Vorticity maximum value variation curve of the wake.

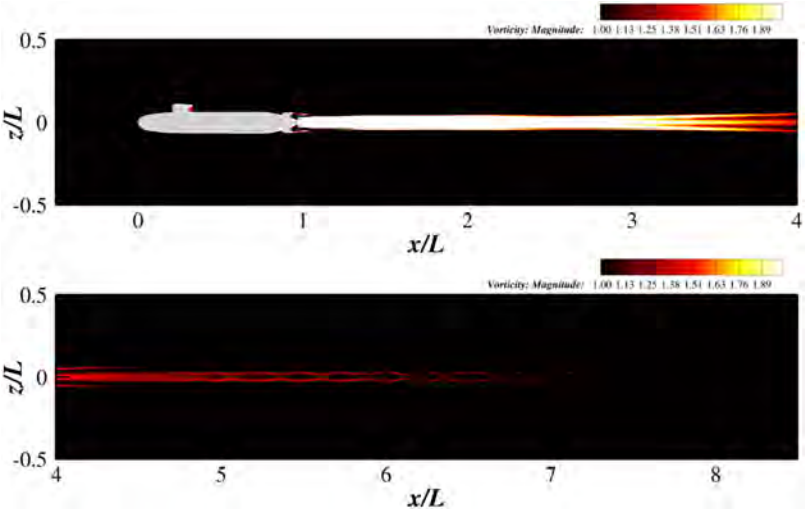

Fig. 15. Vorticity distribution of the wake ($z = 0, 30\,\mathrm{kn}$).

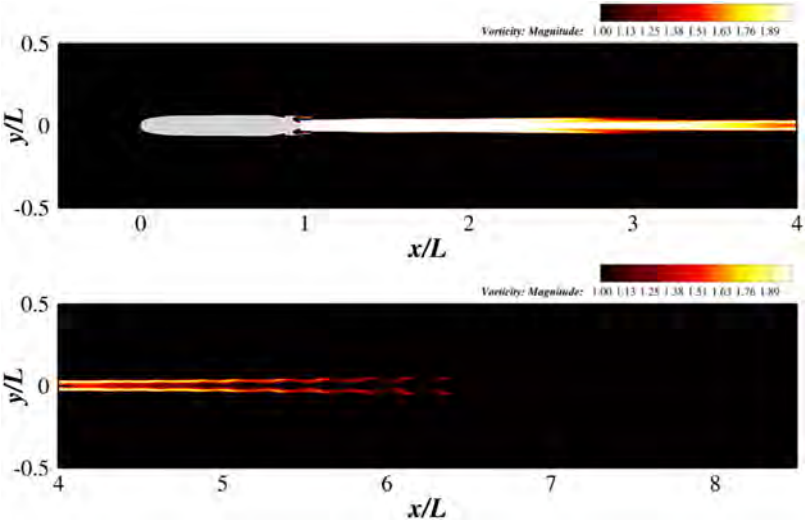

Fig. 16. Vorticity distribution of the wake ($y = 0, 30\,\mathrm{kn}$).

Figure 17 presents the three-dimensional structure of vorticity isosurfaces, set at a value of $0.5\,\mathrm{s}^{-1}$. Upon closer examination of the enlarged local view, it is evident that significant attachment vortices exist on the surface of the underwater vehicle. As the distance from the underwater vehicle increases, the overall shape of the isosurfaces also exhibits a spiraling pattern. Observing the vorticity distribution plots of different sections behind the underwater vehicle in Fig. 18, it can be observed that as the distance increases, the vorticity in the wake gradually decreases.

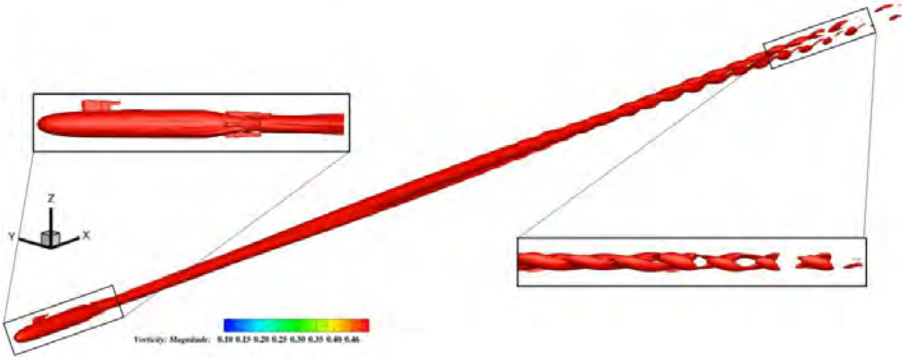

Fig. 17. Vorticity iso-surface of the wake ($w = 0.5$/s, 30 kn).

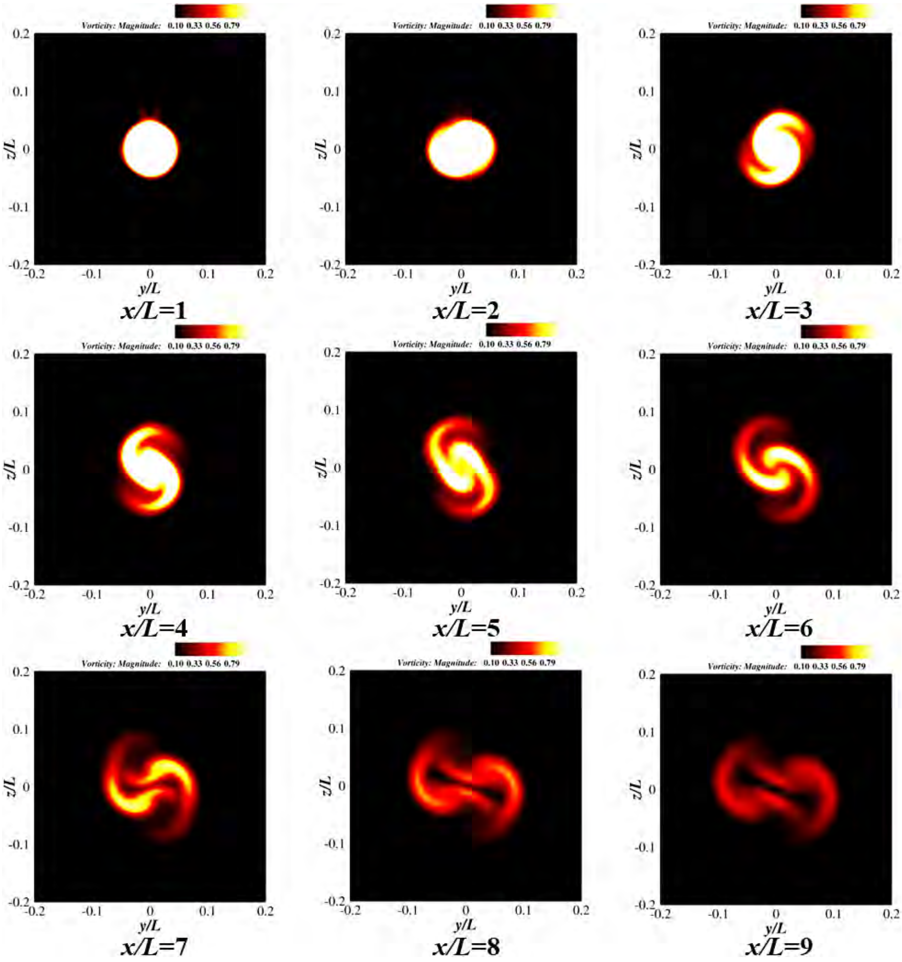

x/L=1 x/L=2 x/L=3
x/L=4 x/L=5 x/L=6
x/L=7 x/L=8 x/L=9

Fig. 18. Distribution of vorticity (30 kn).

4. Conclusions

Based on the RANS method and using the $SST\ k-\omega$ turbulence model, this study conducted numerical simulations of hydrodynamic wakes and thermal wakes at full scale and various cruising speeds, using the SUBOFF model as the subject. The conclusions are as follows:

(a) For the temperature, velocity, and vorticity values in the wake, increase with increasing cruising speed and gradually decrease with increasing distance from the underwater vehicle.
(b) For the temperature and velocity distributions in the wake, the vertical distribution range is greater than the lateral distribution range. The iso-surface of temperature, velocity, and vorticity in the wake exhibit a spiral pattern at greater distances from the underwater vehicle.
(c) For the temperature, velocity, and vorticity distributions at different cross-sections behind the underwater vehicle, the values of these physical quantities decrease as the distance increases, while their influence on the surrounding fluid expands. There are two trailing vortices present, which have a topological relationship with the shape of the propeller.

Acknowledgments

This work is supported by the National Natural Science Foundation of China (52131102), to which the authors are most grateful.

ORCID

Gang Gao https://orcid.org/0009-0005-0081-9459
Liushuai Cao https://orcid.org/0000-0002-0688-2441
Decheng Wan https://orcid.org/0000-0002-1279-3891

References

Cao, L., Gao, G., Guo, E. and Wan, D. [2023] "Hydrodynamic performances and wakes induced by a generic submarine operating near the free surface in continuously stratified fluid," *J. Hydrodyn.* **35**(3), 396–406.

Cao, L., Pan, Y., Gao, G., Li, L. and Wan, D. [2024] "Review on the hydro-and thermodynamic wakes of underwater vehicles in linearly stratified fluid," *J. Mar. Sci. Eng.* **12**(3), 490.

Chen, Q., Xuan, Y., Lin, Q., Han, Y. and Wei, K. [2023] "Evolutions of hydrodynamic and electromagnetic wakes induced by underwater vehicles," *Appl. Ocean Res.* **140**, 103750.

Gu, W., Zhang, J. L., Meng, Q. J., Peng, L., Shen, Z. B. and Deng, H. H. [2018] "Study of underwater vehicle's wake in seawater of linearly gradient temperature and density," *ISOPE Int. Ocean and Polar Engineering Conf.*, pp. ISOPE-I.

Huang, B., Liu, Z., Xu, Y., Pan, M., Hu, J. and Zhang, Q. [2024] "Far-field characteristics and evolutions of electromagnetic field induced by the wake of underwater vehicles," *Appl. Ocean Res.* **145**, 103933.

Li, G., Du, Y. and Yang, L. [2023] "Simulation study on thermal wake characteristics of underwater vehicle under rotary motion," *Appl. Sci.* **13**(3), 1531.

Luo, F., Shuai, C., Du, Y., Gao, C. and Wang, B. [2024] "Experimental on the thermal characteristics of surface wake generated by submerged vehicle," *Ocean Eng.* **297**, 116957.

Luo, F., Shuai, C., Du, Y. and Ma, J. [2022] "Numerical simulation of temperature variation in water layer induced by thermal jet in weak stratified environment," *AIP Adv.* **12**(6), 065222.

Luo, F., Shuai, C., Du, Y. and Ma, J. [2023] "Thermal characteristics of vehicle wake induced by the interaction between hydrodynamic wake and cold skin," *Ocean Eng.* **267**, 113272.

Wang, C. A., Xu, D. and Gao, J. P. [2023] "Surface temperature characteristics of underwater thermal jet based on thermal skin," *Appl. Ocean Res.* **130**, 103411.

Zhang, X., Guo, L., Hu, R. and Liu, C. [2019] "Cold-thermal wake characteristics of submarine in temperature-density stratified seawater," *Fifth Symp. Novel Optoelectronic Detection Technology and Application*, Vol. 11023, pp. 1293–1298.